LANGMUIR

pubs.acs.org/Langmuir Article

Rayleigh-Taylor Instability in Soft Viscoelastic Solids

Published as part of Langmuir virtual special issue "Highlighting Contributions from our Editorial Board Members in 2023".

Malcolm Slutzky, Jonghyun Hwang, Howard A. Stone,* and Janine K. Nunes*



Cite This: Langmuir 2024, 40, 1567–1575



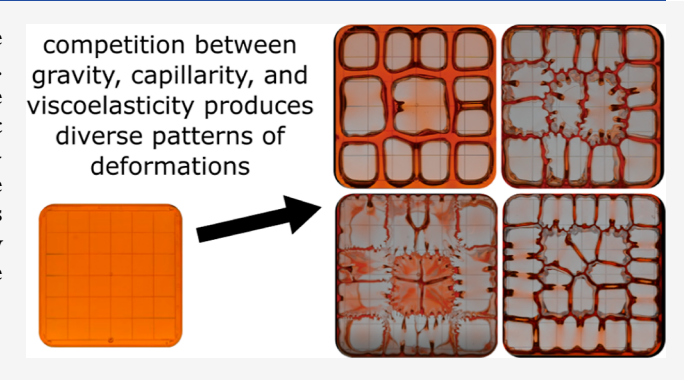
ACCESS I

III Metrics & More

Article Recommendations

s Supporting Information

ABSTRACT: We present an experimental characterization of the gravity-driven Rayleigh—Taylor instability in viscoelastic solids. The instability creates periodic patterns on the free surface of the soft solids that are distinct from the previously studied elastic Rayleigh—Taylor instability. The experimental results are supported by the linear stability analysis reported here. We identify the dependence of the steady-state pattern of deformations on the gel's geometry, complex shear modulus, and surface tension. This study provides quantitative measures applicable to the design of tunable surface textures, soft machines, and 3D structures.



■ INTRODUCTION

Viscoelastic gels exhibit properties of elastic solids and viscous liquids depending on the mechanical conditions and the timescale over which stress is applied. Some gels can recover from damage or fracture, 1,2 have strong adhesive properties, 3-5 and/or exhibit various surface instabilities and patterns, 6-8 which are all functions of the composition of the gel. One way to create a pattern on the surface of "soft" materials is via the Rayleigh-Taylor instability, which is typically associated with the instability at the interface of two fluids of different densities due to the competition between gravitational, inertial, capillary, and viscous effects. 9,10 Similar dynamics can occur with elastic materials. Hence, the Rayleigh-Taylor instability can cause the surface of liquids and gels¹¹ to form a wavy pattern when the free surface of a material is oriented downward so that it is deformed in the direction of gravity. Specifically, gravity-driven deformations on soft gels often appear as a periodic pattern of dimples with a characteristic wavelength determined by the shape, size, and chemical and mechanical properties of the material; in some cases, the patterns are reversible upon inverting the sample, while in other cases, there is irrecoverable strain.

Initially, the Rayleigh—Taylor instability was recognized as a phenomenon occurring at the interface of a Newtonian liquid and a gas or two Newtonian liquids. Numerous theoretical studies have appeared over the decades to discuss the Rayleigh—Taylor instability in viscoelastic liquids. Recently, a new feature of the instability—the existence of a steady-state pattern of deformations—was identified by several research groups that experimentally characterized the Rayleigh—Taylor instability in elastic solids. 11,17,18 In addition,

several groups have developed theoretical models of the Rayleigh—Taylor instability in viscoelastic solids. ^{19,20} However, to the best of our knowledge, there has not yet been experimental research specific to the Rayleigh—Taylor instability in viscoelastic solids, which is the goal of this paper.

Therefore, we experimentally study the Rayleigh—Taylor instability for initially planar configurations of viscoelastic gels of various material properties and thicknesses. We investigate the effects of viscoelasticity and capillarity. In addition, using linear stability analysis, we identify four dimensionless groups that affect the onset of pattern formation and the typical wavenumber, allowing us to predict and characterize the Rayleigh—Taylor instability-driven surface waves and deformation wave modes. By analyzing the images of deforming gels, we are able to describe the time development of the pattern and, in the case of a steady-state pattern possible with viscoelastic solids, the geometry of the stable deformed surface.

EXPERIMENTAL PROCEDURE

Material Fabrication and Experiment. The viscoelastic gels we used consist of vinyl-terminated polydimethylsiloxane (PDMS, Gelest), silicone oil (Sigma-Aldrich), a cross-linker, and a catalyst. The catalyst was platinum-divinyltetramethyldisiloxane complex, 2% Pt in xylene (Gelest), and we used (25–35% methylhydrosiloxane)—

Received: August 31, 2023 Revised: November 17, 2023 Accepted: November 21, 2023 Published: December 19, 2023





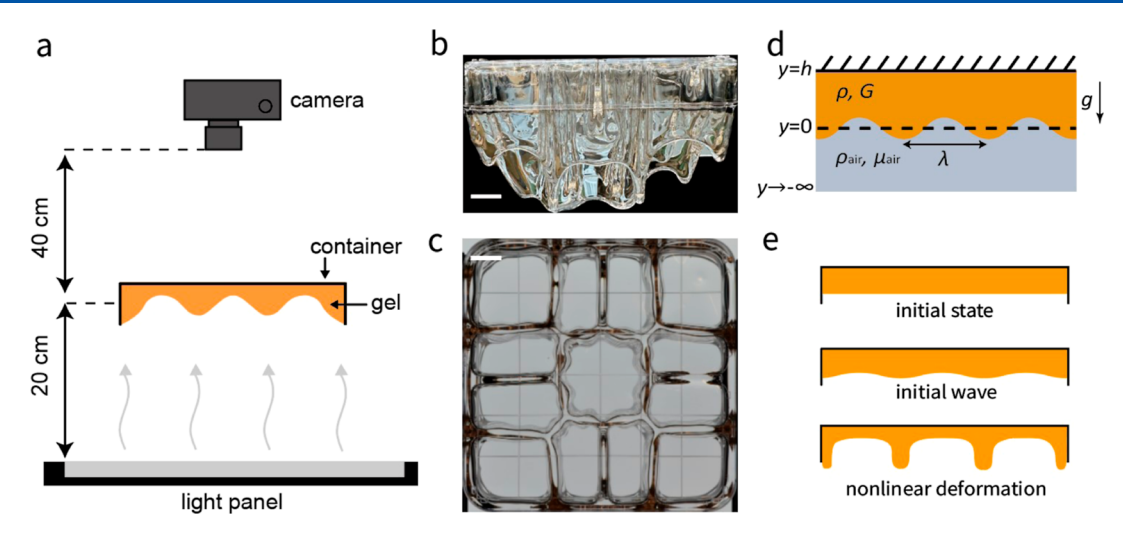


Figure 1. Instability of a viscoelastic gel. (a) Schematic of the experimental setup. (b,c) Inverted viscoelastic gel at steady state, shown in the (b) side view and (c) top view. Scale bars are 10 mm. (d) Schematic representation of the Rayleigh—Taylor instability. A viscoelastic gel of density ρ , dynamic modulus G, and thickness h is placed on top of air with density ρ_{air} and viscosity μ_{air} . For sufficiently soft gels, a characteristic perturbation of the wavelength λ develops along the gel—air interface. (e) Material flows and deforms under the influence of gravity. Deformations of a characteristic wavelength develop while the material tries to maintain its shape through elastic and capillary forces.

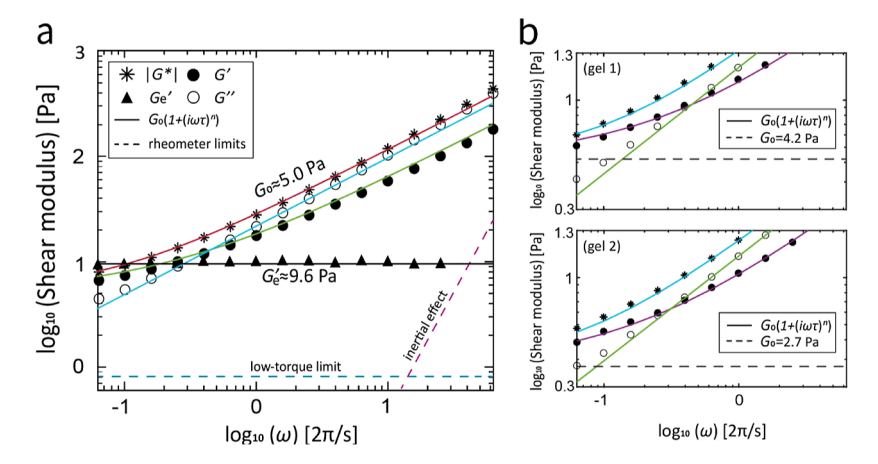


Figure 2. Rheological characterization of select elastic and viscoelastic gels. (a) Star: $|G^*|$; circle: viscoelastic; triangle: elastic; filled: storage modulus; and empty: loss modulus. Subscript "e" stands for the hydrogel. The storage modulus of the hydrogel was measured constant at $G_e' \approx 9.6$ Pa at all frequencies tested. Hence, we consider the hydrogel as an elastic solid. The rubbery plateau modulus of the viscoelastic gel G_0 was fitted with the following function: $G^* = G_0[1 + (i\omega\tau)^n]$. Images of gels with these material properties are provided in Figure 4b. (b) Gels with different cross-linker concentrations, c_c . (Top) 0.10 Pa·s silicone oil with 0.244 wt % c_c . $G_0 = 4.2$ Pa, $\tau = 8.8$ s, and n = 0.68, and (bottom) 0.35 Pa·s silicone oil with 0.233 wt % c_c . $G_0 = 2.7$ Pa, $\tau = 14$ s, and n = 0.67. We call the top and bottom gels, gel 1 and gel 2, respectively. Images of gels with these material properties are provided in Figure 5a.

dimethylsiloxane copolymer, trimethylsiloxane terminated, 25–35 cSt (Gelest) as a cross-linker. The mass ratio between PDMS and silicone oil was 1:1. This liquid-filled polymer network is known to produce gels with tunable viscoelastic properties. ^{21,22} Depending on the desired gel composition, we used silicone oils with dynamic viscosities of $\mu=0.019,\,0.096,\,$ and 0.338 Pa·s (reported by the manufacturer). For each sample, 0.0077 wt % of catalyst was added. The weight percent of the catalyst was kept constant to maintain a relatively uniform rate of polymerization between experiments. The cross-linker concentration, c_{cl} ranged from 0.225 to 0.248 wt %, based on the desired mechanical properties of the gel. For imaging purposes, select viscoelastic gels were prepared with a small amount of oil-compatible fluorescent dye (Dye-Lite) in a 1:62 mass ratio between dye and silicone oil. The addition of dye was the only difference between the dyed and undyed gels prepared in this study. All materials were used as received.

To form the viscoelastic gels, all components were mixed thoroughly and poured into square Petri dishes (with side lengths of either 115 or 90 mm). The mixture was then degassed in a vacuum

chamber. Next, the mixtures were cured overnight in an \approx 63 °C oven. The gels were then brought to room temperature (23–25 °C).

To highlight the differences in the Rayleigh—Taylor instability in various classes of materials, we also produced elastic Rayleigh—Taylor instability in agarose-based hydrogels. To form the hydrogel, powdered agarose (Invitrogen) was added to deionized water such that the final mixture was 0.08 wt % agarose. We then boiled the mixture and poured it into rectangular Petri dishes (side length 210 mm and width 60 or 40 mm). The Petri dishes were covered with a lid to prevent evaporation and were left to cure at room temperature for 6 h.

The experimental setup is illustrated in Figure 1a. For imaging, a Nikon D5100 camera with a Nikon DX18—55 mm lens was used. All gels are transparent, so we were able to capture the deformation by imaging from above. Fully cured gels were initially planar and flat. They were quickly inverted in the air and placed above a light panel. Images of a fully deformed gel are provided in Figure 1b,c.

Material Characterization. To quantitatively characterize the flow behavior of the viscoelastic gels, we performed shear rheology

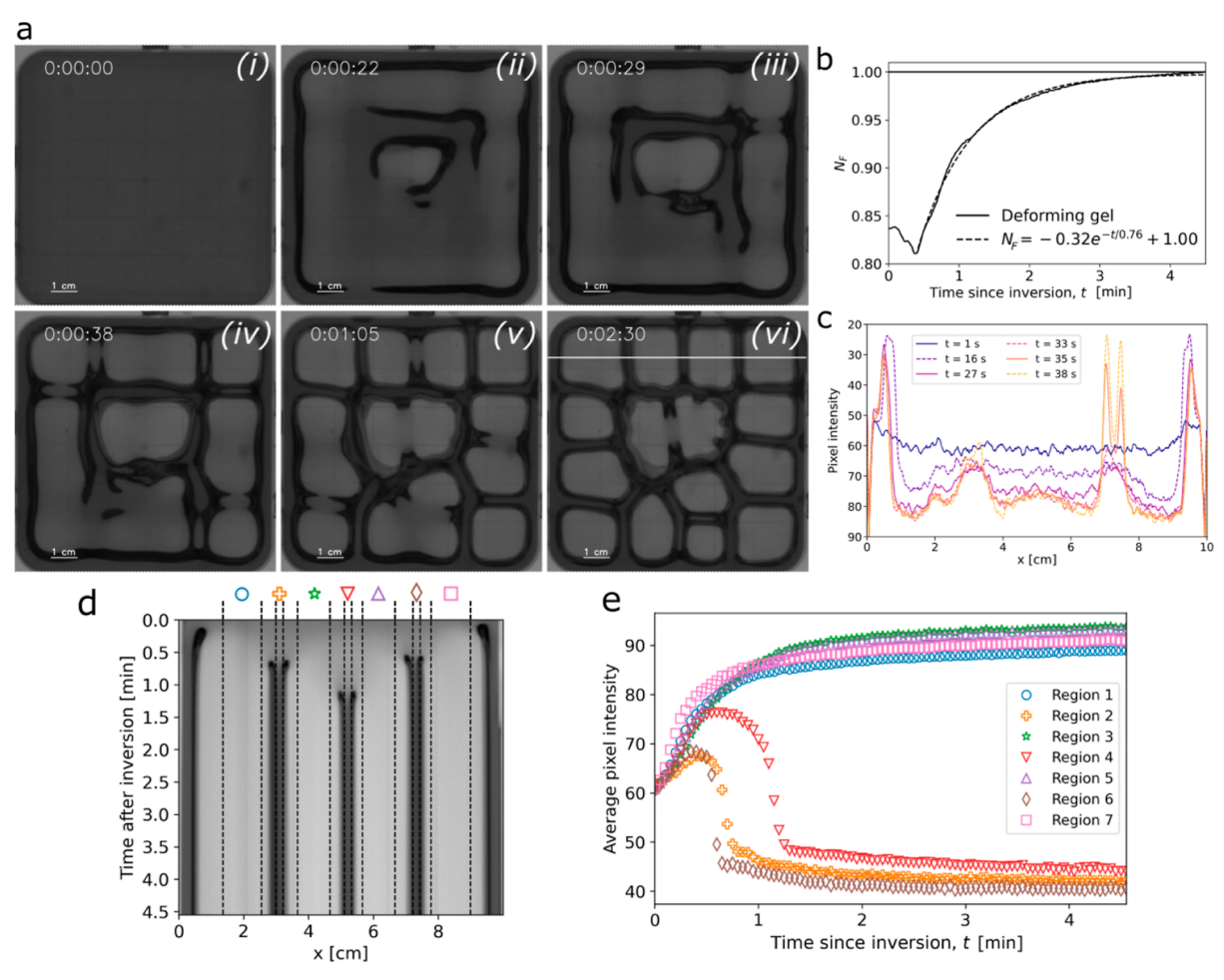


Figure 3. Development of the viscoelastic Rayleigh—Taylor instability. (a) Images of a viscoelastic gel at various times throughout its deformation, where the time after inversion of the Petri dish is indicated as hr:min:s. (b) Normalized Frobenius norm N_F of all of the pixel intensities in each gel image as a function of time since inversion. N_F is plotted with a solid line, and the line of best fit is plotted with a dashed line. (c) Overlaid intensity profiles of the slice (white line) indicated in image (vi) at various times during the first 38 s of deformation. The profiles were smoothed with a moving average. (d) Kymograph of the indicated slice throughout the gel's evolution. The state of the gel slice immediately after inversion is shown at the top of the figure, and the bottom of the figure refers to the slice at a steady state. Seven regions, labeled at the top of the figure, are marked with vertical dashed lines going through the kymograph. (e) Average intensity of the seven regions indicated in (d) as a function of time. After a sharp decrease in the intensity of dark regions, the gel gradually reaches its steady-state pattern.

using a parallel plate rheometer (Anton Paar, MCR 302e) to measure their storage modulus, G', and loss modulus, G''; see Figure 2. To minimize slip of the oil-based material on the top and bottom plates, we executed the measurements with a sand-blasted parallel plate of 50 mm diameter and a 1.0 mm gap between the plates. In particular, the gels were fully cured in the oven, loaded onto the rheometer, allowed to reach room temperature, and then measurements were made using a constant shear strain $\gamma = 0.1\%$; the variable frequency f was logarithmically increased from 0.01 to 10 Hz.

To measure the rheological properties of the hydrogels, which were essentially elastic solids, we pipetted an uncured solution of 0.08 wt % agarose onto the rheometer. The solution was left to reach room temperature so that it would fully cure. Once the solution was fully cross-linked, we executed measurements using constant shear strain γ = 0.1%, and variable frequency f logarithmically increased from 0.01 to 10 Hz. We denote the storage and loss moduli of hydrogels as $G_{\rm e}'$ and $G_{\rm e}''$, respectively. $G_{\rm e}'$ is plotted in Figure 2; we were unable to accurately measure $G_{\rm e}''$ due to the low-torque limit of the rheometer.

The rheological measurements provided G' and G''. The relaxation time, $\tau_{\rm m}$, was taken to be the inverse of the crossover frequency, where the crossover frequency is defined as the frequency at which G' = G''. Generally, as the cross-linker concentration $c_{\rm c}$ increased, the complex modulus of the gel increased and $\tau_{\rm m}$ decreased. Similarly, for two

viscoelastic gels with the same c_c but different silicone oil viscosity, μ , gels with higher μ had a larger complex shear modulus.

To simply describe the dynamic modulus, we follow ref 23 and approximate the complex modulus $(G^* = G' + iG'')$ with a power-law model in the form of $G^* = G_0[1 + (i\omega\tau)^n]$ to fit to the rheological measurements. G_0 is interpreted as the rubbery plateau modulus, ω is the angular frequency of the shear $(\omega = 2\pi f)$, τ is the fitted relaxation time, and n is the power-law exponent. More details on the rheological characterization can be found in the Supporting Information. We observed that the relaxation time τ_m and the fitted time scale τ are similar in magnitude but not exactly the same. The fitted shear flow characteristics were then used to predict the Rayleigh—Taylor instability-driven deformations on the gels. Rheological characterization of select viscoelastic gels is provided in Figure 2. We note that the PDMS gels are viscoelastic solids, as the low frequency, long-time response has G' > G''.

In our study, we approximate the surface stress of the partially cross-linked viscoelastic gel to equal the surface tension γ of uncured PDMS ($\gamma \approx 21 \times 10^{-3}$ N/m), due to the gel's large sol fraction. ^{24,25} Surface stress is defined as the energy per unit area required to stretch a soft interface into a different shape. For liquids, the surface stress and surface tension are equal. The surface stress has been used in many works in the literature to account for the surface properties of soft materials. ^{21,26}

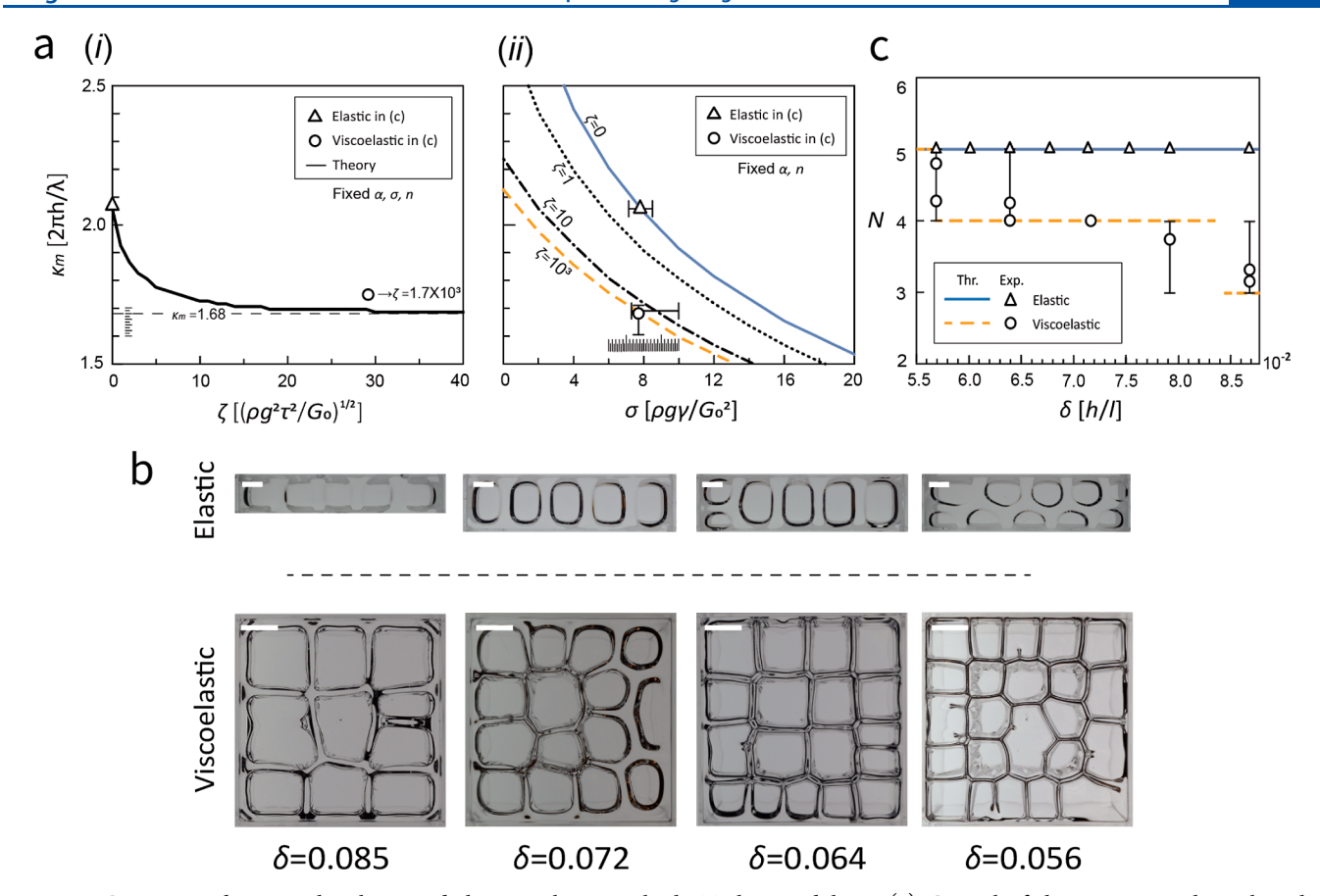


Figure 4. Comparison between the elastic and the viscoelastic Rayleigh–Taylor instabilities. (a) Control of the parameters that select the wavenumber. (i) Most unstable wavenumber $\kappa_{\rm m}$ for a fixed $\alpha=\rho gh/G_0\approx 13.7$, $\sigma=\rho g\gamma/G_0^2\approx 7.7$, and n=0.65 starts from $\kappa_{\rm m}\approx 2.07$ and decreases to $\kappa_{\rm m}\approx 1.68$ as the viscoelastic relaxation time τ increases. (ii) Dependence of $\kappa_{\rm m}$ on σ . Increasing σ stabilizes the interface, decreasing $\kappa_{\rm m}$. The circle and triangle markers in parts (i) and (ii) represent experimental data points from (c). (b) Experimental observations of the most unstable wave mode $N=\kappa_{\rm m}/(2\pi\delta)$ versus aspect ratio $\delta=h/l$. For this range of δ , the elastic gels constantly have N=5, whereas the viscoelastic gels transition from N=3 to N=5 as δ decreases. Scale bars are 20 mm. Rheological characterization of these gels is provided in Figure 2a. (c) Experimental observation is supported by the linear stability model. Lines are the linear stability theory, and markers are the experiments. The wave mode N from the experiment is the square root of the number of deformed regions. Error bars indicate the max/min number of deformed regions in one direction in a gel; e.g., the bottom right gel in (b) has $N_{\rm max}=5$, $N_{\rm min}=4$, and $N\approx 4.8$.

RESULTS AND DISCUSSION

Development of the Rayleigh-Taylor Instability. To visualize the development of the instability, we dyed a gel (μ = 0.019 Pa·s, $c_c = 0.260$ wt %, initial thickness h = 6 mm, and 0.8 wt % dye) and measured the intensity of light transmitted through the gel by recording images while it deformed. The gels, cast and cured in a Petri dish, were initially flat, and the interface became unstable upon inversion of the Petri dish. The pixel intensities in the images, which vary both spatially and temporally, are a qualitative indicator of the relative thickness of the gel, where higher intensities correspond to thinner regions, and decreasing pixel intensity generally indicates increasing thickness. We note that highly curved regions of the gel tend to appear as the lowest pixel intensities in the images but do not reflect the relative thickness of those regions; rather, these are regions of rapid shape change of the gel.

A time series of images of a representative dyed gel sample during deformation is provided in Figure 3a. We denote h and l as the initial thickness of the gel and the side length of the container, respectively. Immediately after inversion, the gel appeared mostly undeformed with a uniform thickness [Figure 3a(i)]. One of the first inhomogeneities occurred along the

perimeter of the gel, where the gel slid down along the side walls of the dish, as seen by the dark line around the outside of the gel, suggesting a region of high curvature [Figure 3a(ii)]. This change was accompanied by thinning in other areas of the gel, specifically, the high pixel intensity regions close to the gel's perimeter and at the gel's center. The thinning in the gel's center was partially encircled by a border of dark intensity, indicating a rapid change in the gel's thickness. These deformations became more pronounced by 29 s, as a grid-like pattern started to form [Figure 3a(iii)]. For the square-shaped containers, we use this "grid" of deformed regions to define the dimensionless wave mode $N=l/\lambda$, where the wavelength λ refers to the size of the grid. Due to the variation in size and shape of the deformed regions, the majority of our analysis will focus on N.

As time progressed, the grid pattern became more well defined, and each thin deformed region was bordered by narrow regions of dark intensity, indicating that these regions were separated from each other by long hanging sections of the gel [Figure 3a(iv-vi)]. By 2.5 min, the pattern had almost reached a steady state, exhibiting a dominant wave mode of $N \approx 4$ [Figure 3a(vi)]. For each experiment in the square containers, we counted the number of distinctly deformed regions and reported the square root of that number as N.

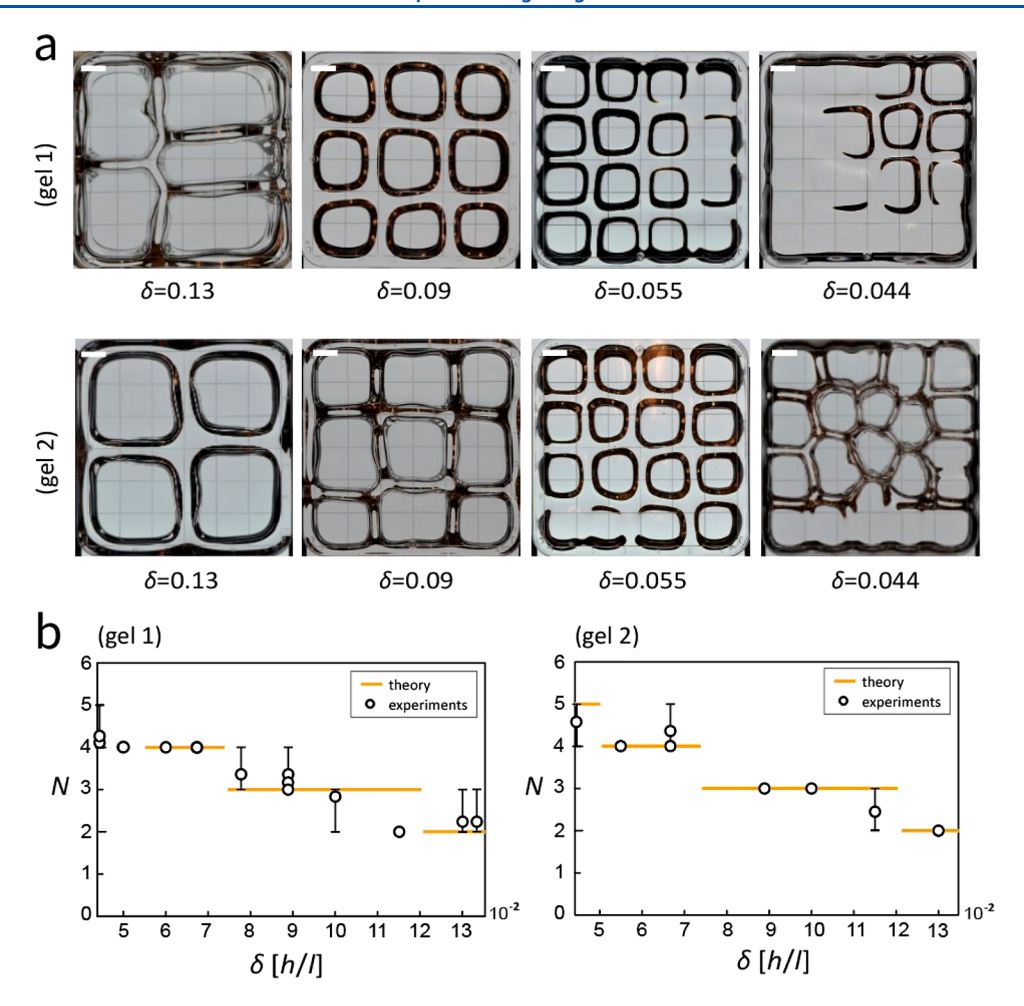


Figure 5. Influence of the gel thickness on wave mode selection. (a) Gels at four different aspect ratios $\delta = h/l = 0.13$, 0.09, 0.055, and 0.044. Scale bars are 10 mm. Rheological characterization is provided in Figure 2b, with gels 1 and 2 described by the top and bottom plots of Figure 2b, respectively. (b) Comparison between the experimental observations and the linear stability model. Rheological characterization of the material gives predictions of the shape mode at each aspect ratio δ .

From the time series of images, we observed that the amplitude changed at different rates in different locations on the surface of the gel.

To quantitatively represent the overall state of the gel pattern at every time point, we calculated the time-dependent normalized Frobenius norm, $N_F(t) = ||P||_F/||P(t = t_f)||_F$, shown in Figure 3b. Each image of a deforming gel was converted to a matrix of pixel intensities, p_{ij} , and the norm of the pixel intensity matrix was calculated with the equation $\|P\|_{\mathbb{F}} = (\sum_{i,j} (p_{ij})^2)^{1/2}$. Normalization was achieved by dividing by $||P||_F$ at the gel's steady state, time $t = t_{tr}$ such that $N_F \rightarrow$ 1 at large times. More details on $N_{\rm F}$ are provided in the Supporting Information. After the first ≈ 30 s of the gel's deformation, $N_{\rm F}(t)$ was best fitted by an exponential function in time of the form $N_{\rm F}(t) = a \, {\rm e}^{-t/\tau_{\rm b}} + b$, where we define $\tau_{\rm b}$ as the characteristic time describing the rate of change of the gel's bulk deformation. Consequently, some aspect of the gel's overall deformation can be captured over a single characteristic time (in this case, $\tau_b = 0.76$ min). When considering the fitted relaxation time au and viscous relaxation time au_{m} defined in the previous section, softer gels (smaller G'), with larger τ or $\tau_{\rm m}$, tend to deform faster (see Figure 6c below), leading to lower $\tau_{\rm b}$.

To better understand the evolution of a viscoelastic gel to a steady state, we analyzed the time dependence of a specific slice of the deforming gel, indicated by the white horizontal line in Figure 3a(vi). The pixel intensities along this slice are shown for different times in Figure 3c and indicate that the rate of deformation was spatially nonuniform, as expected, as nonlinearity influences the shape changes. We also note that this reconstructed profile is not an exact profile of the deformed gel.

The deformation dynamics within a specified slice can also be represented by a kymograph, as shown in Figure 3d. Each row of pixels in the kymograph gives the slice at a different time in the gel's deformation history. Seven regions are labeled at the top of the plot, and their corresponding pixel intensities are shown in Figure 3e. In agreement with features evident in Figure 3c, the formation of two distinct low-intensity (long-hanging) regions occurred between 0.5 and 1 min. The kymograph also shows the later development of a third long-hanging region going through the center of the slice. The trends of the thin gel regions, plateauing at high pixel intensity, can be fit to exponentially decaying functions in time, with characteristic times ranging from 0.43 to 0.61 min. These characteristic times are comparable to but less than the characteristic time of the gel's overall deformation determined

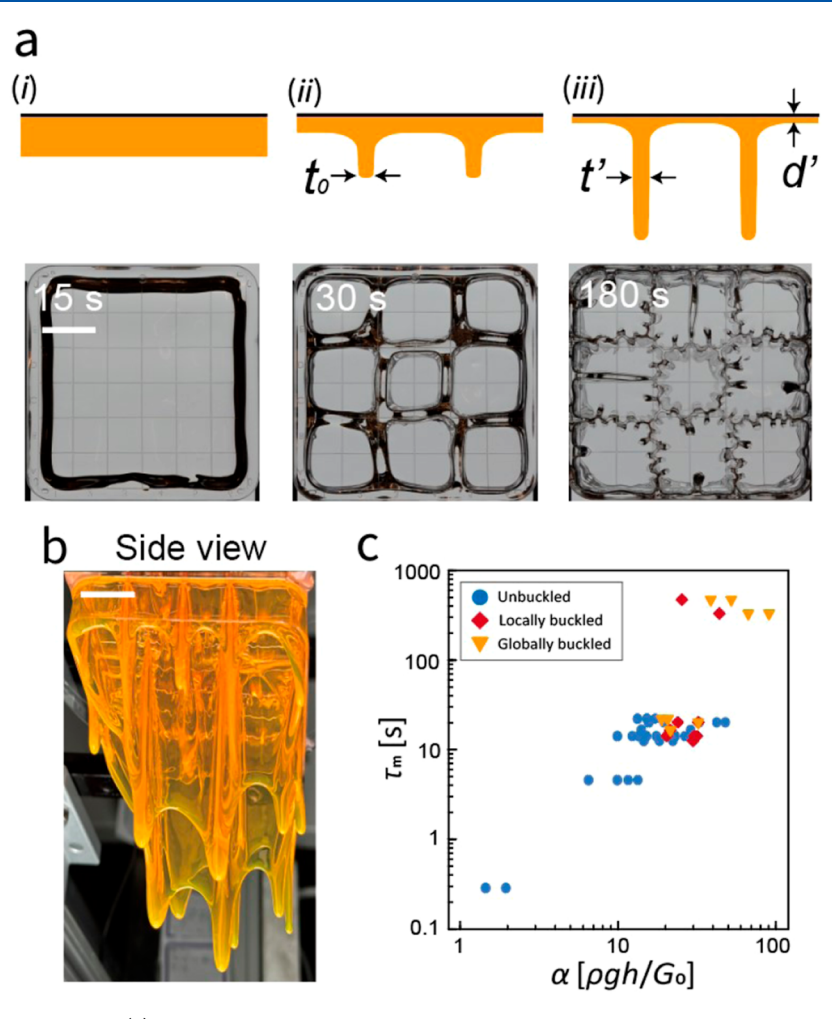


Figure 6. Secondary buckling instability. (a) Potential mechanism of secondary buckling. Sections of the soft gel flow downward over time (i–iii) and a larger portion of its mass is then supported by a decreased contact area. (i) Onset of Rayleigh–Taylor instability, (ii) gel deformation enters nonlinear growth, and (iii) the system develops tension, which manifests in wrinkling instability. (b) Typical gel that displays secondary buckling seen from the side at its maximum stretch, equivalent to the state described in (a iii). Scale bars are 20 mm. (c) $\alpha = \rho gh/G_0$ versus τ_m , with gels labeled according to the presence of secondary buckling in their steady-state pattern of deformations. τ_m is the inverse of the crossover frequency and is interpreted as the relaxation time. Circles indicate no secondary buckling; diamonds indicate the onset of secondary buckling, and triangles indicate globally buckled gels.

from $N_{\rm F}$ in Figure 3b. One may notice that regions 2 and 6 in Figure 3e develop earlier than region 4. In the experiment, the larger cells appear first, and then the smaller cells emerge, which is due to the boundary effect; the gel deforms first in the regions near the boundary.

Viscoelastic Linear Stability Model. Having discussed the Rayleigh—Taylor instability-driven pattern formation within a single viscoelastic gel, we next characterize the relationships between a gel's material properties and its resulting pattern of deformations. We performed a linear stability analysis to identify the parameters that affect the deformation and quantitatively predict the most unstable wavenumber. A reader not interested in the mathematical details can skip this section and proceed directly to the results.

The initially planar gel—air interface becomes unstable over time due to gravitational forces. For a material with density ρ (and neglecting the density of air), surface tension γ , viscosity μ , relaxation time τ in a container of length l where the gel has thickness h, and gravitational acceleration g, we write the linearized momentum equation, incompressibility relation, and constitutive equation for the stress versus rate-of-strain relation as

$$\rho \frac{\partial u_i}{\partial t} = -\frac{\partial p}{\partial x_i} + \frac{\partial \sigma_{ij}}{\partial x_j} - \rho g_i$$
(1a)

$$\frac{\partial u_i}{\partial x_i} = 0$$
 (1b)

$$\sigma_{ij} = \mu \dot{\varepsilon}_{ij} = \mu \left(\frac{\partial u_i}{\partial x_j} + \frac{\partial u_j}{\partial x_i} \right)$$
 (1c)

where p is the pressure field, σ_{ij} and ε_{ij} are the stress and strain tensors, respectively, and u_i is the velocity component in the ith direction. Below, we will allow the viscosity to be a function of the time scale of deformation, but it is independent of the spatial position. Next, we look for the solutions with frequency ω and so define $\mu i \omega = G^*(\omega)$.

In the formulation of the linear stability problem, we assume a two-dimensional configuration, e.g., $u_z(x, z, t)$, seek the form of the solution as $u_z(x, z, t) = U_z(z) e^{i\omega t} e^{ikx} = (A e^{-kz} + B e^{kz} + C e^{-mz} + D e^{mz}) e^{i\omega t} e^{ikx}$ with unknown coefficients A, B, C, and D, along with frequency ω and the wavenumbers $k = 2\pi/\lambda$ and

 $m = \sqrt{k^2 - (\rho \omega^2)/G^*(\omega)}$; the corresponding growth rate is Re{i ω }. We write no-slip and kinematic boundary conditions on the solid boundary (z = h) and normal and tangential stresses on the free interface, respectively, as z^{27}

$$U_z(h) = 0 (2a)$$

$$\left. \frac{\mathrm{d}U_z}{\mathrm{d}z} \right|_{z=h} = 0 \tag{2b}$$

$$\left[\rho + \frac{G^*}{\omega^2} \left(\frac{\mathrm{d}^2}{\mathrm{d}z^2} - k^2\right)\right] \frac{\mathrm{d}U_z}{\mathrm{d}z} \bigg|_{z=0}$$

$$= \frac{k^2}{\omega^2} (\rho g - k^2 \gamma) U_z \bigg|_{z=0} + 2k^2 \frac{G^*}{\omega^2} \frac{\mathrm{d}U_z}{\mathrm{d}z} \bigg|_{z=0}$$
(2c)

$$\left(\frac{\mathrm{d}^2}{\mathrm{d}z^2} + k^2\right) U_z \bigg|_{z=0} = 0 \tag{2d}$$

Note that the last two boundary conditions address the continuity of the normal and tangential stresses at the perturbed interface $z=\eta(x,t)$, where $\partial\eta/\partial t=u_z|_{z=0}$. For small deformations, the pressure discontinuity at the interface can be approximated as $\gamma\partial^2\eta/\partial x^2$, which gives the $-k^2\gamma$ term in eq 2c. A nontrivial solution to the system of equations that results from applying these boundary conditions exists only when the corresponding determinant of the coefficient matrix C is set to zero: $\det(\mathbf{C})=0$. The detailed derivation is described in the Supporting Information. We determine a dimensionless form of this solvability condition, using $G^*=G_0[1+(\mathrm{i}\omega\tau)^n]=\mu\mathrm{i}\omega$, and dimensionless parameters $\alpha=\rho gh/G_0$, $\sigma=\rho g\gamma/G_0^2$, and $\zeta=\sqrt{\rho g^2\tau^2/G_0}$, in the form

$$\kappa \xi(\kappa^{2} - \xi^{2}) \frac{\alpha - \kappa^{2} \sigma / \alpha}{(1 + (i\tilde{\omega}\xi / \alpha)^{n})} \cosh \xi \sinh \kappa$$

$$-\xi (5\kappa^{4} + 2\kappa^{2}\xi^{2} + \kappa^{4}) \cosh \kappa \cosh \xi$$

$$-\kappa^{2} (\kappa^{2} - \xi^{2}) \frac{\alpha - \kappa^{2} \sigma / \alpha}{(1 + (i\tilde{\omega}\xi / \alpha)^{n})} \cosh \kappa \sinh \xi$$

$$+4\kappa^{2}\xi (\kappa^{2} + \xi^{2}) + \kappa (\kappa^{4} + 6\kappa^{2}\xi^{2} + \xi^{4}) \sinh(\kappa) \sinh(\xi) = 0$$
(3)

which gives the dimensionless wavenumbers $\kappa = kh = 2\pi h/\lambda$ and $\xi=mh=\sqrt{\kappa^2-\tilde{\omega}^2/(1+(i\tilde{\omega}\zeta/\delta)^n)}$ as a function of the dimensionless growth rate $\tilde{\omega} = \sqrt{\rho h^2 \omega^2/G_0}$, through dimensionless parameters α , σ , ζ , and δ . Here, α relates the geometry (h) and the rubbery plateau modulus (G_0) and, through g, is the driving parameter for the Rayleigh-Taylor instability, i.e., a ratio of gravitational to elastic stresses. ^{11,19} Next, σ relates the surface stress (γ) to the shear modulus of the gel. In the case where the thickness of the gel is much larger than the elastocapillary length of the system, i.e., $h \gg \gamma/G_0$, σ can be neglected, and the analysis of the system can be simplified.^{11,21} ζ , which is the viscoelasticity parameter, compares the viscoelastic relaxation time to the elasto-gravity time scale $(\rho g^2/G_0)^{1/2}$. We note that one recovers the result given by Mora et al. 11 by setting $\sigma = 0$ and $\zeta = 0$. Lastly, δ is the aspect ratio of the gel and is defined as h/l, where l is the length of the container.

Effect of Viscoelastic Properties on the Pattern Selection. We first consider the effect of the viscoelastic

parameter ζ on the most unstable wavenumber $\kappa_{\rm m}$ [Figure 4a(i)]. The model suggests that $\kappa_{\rm m}$ decreases rapidly and then saturates to a minimum value specific to each combination of the other parameters $(\alpha, \sigma, \text{ and } n)$. In this calculation, we used $\alpha=13.7, \ \sigma=7.7, \ \text{and} \ n=0.65$. The most unstable wavenumber at the elastic limit $(\zeta=0)$ is $\kappa_{\rm m}\approx 2.07$ and then decreases to $\kappa_{\rm m}\approx 1.68$ with increasing ζ . This result suggests that the Rayleigh–Taylor mechanism will develop a shorter wavelength λ in elastic gels in comparison to that in viscoelastic solid gels. We then investigate the effect of surface tension on the most unstable wavenumber [Figure 4a(ii)]. We observe that for both elastic and viscoelastic gels, increasing $\sigma=\rho g\gamma/G_0^2$ decreases $\kappa_{\rm m}$. This result was anticipated, as the surface stress acts to stabilize the interface against deformation.

To experimentally test the above predictions, we prepared elastic and viscoelastic gels with equal α and σ . The value of σ was fixed throughout the entire experiment, while we chose four different aspect ratios (δ) of the gels to vary α , as shown in Figure 4b (α and δ are related through the gel thickness, h). Specifically, we have conditioned the surface tension parameter σ of both the elastic and viscoelastic gels to be as close as possible to σ = 7.7. In the Supporting Information, we provide values of all of the parameters that we conditioned to experimentally produce the viscoelastic effect in the Rayleigh—Taylor instability. Note that the values of α and σ are at most within $\pm 1.5\%$ of their mean values (between elastic and viscoelastic), while the ζ parameter is varied significantly. Unfortunately, we were limited by the choice of our material to achieve either $\zeta \approx 0$ or $\zeta \approx O(10^3)$.

Elastic and viscoelastic gels with $\sigma \approx 7.7$ and four values of δ are shown in Figure 4b. Elastic gels exhibited N=5 for all δ , while viscoelastic gels exhibited varying wavenumber N, ranging from 3 to 5. A comparison is made in Figure 4c between the model and the experiments. Note that we observed 5×1 or 5×2 grid patterns with the hydrogels cast in the longer aspect ratio rectangular containers. For that geometry, we also performed two separate linear stability analyses in the length (210 mm) and the width (40 or 60 mm) directions and the model predicted 5 cells and 1–2 cells, respectively. Hence, we believe that the length ratio did not govern the resulting 5×1 pattern. These results confirm that the linear stability model (eq 3) is a reliable tool to predict the wavelength of the pattern that develops on the free surface of hanging soft solid materials.

Effect of Gel Thickness on the Pattern Selection. We next investigated the effect of gel thickness on the steady-state pattern selection. This effect is only manifested through the parameters α or δ . The linear stability model (eq 3) suggests that the characteristic wavelength decreases as the slab thickness decreases. We chose two examples of the gel composition to investigate how the wave modes differed as we varied the aspect ratio of the gels (Figure 5a). As shown in Figure 4a, all viscoelastic gels in this study had the ζ parameter far from the elastic limit. Hence, the ζ and σ parameters were set constant in the experiments in Figure 4a and only the thickness was varied. By comparing Figure 5b(i,ii), we observe that the α parameter governs the onset of the instability.¹¹ Surface tension also affects the stability of thinner gels $(h \sim \gamma/$ G_0), as the surface tension tries to stabilize the interface. In our experiments, the elastocapillary length was $\gamma/G_0 \approx 5-7$ mm, meaning that gels thinner than h < 5 mm were less likely to deform. Although the gels in Figure 5a(i,ii) had different rubbery plateau moduli ($G_{0(i)} \approx 4.2 \text{ Pa}$ and $G_{0(ii)} \approx 2.7 \text{ Pa}$), the

thickness of the gel had a stronger influence on the selection of the wavenumber.

Tension-Induced Surface Instability in Viscoelastic Gels. In very soft gels, the wave amplitude grew substantially; for example, the typical amplitude of the long-time deformation ranges from less than 1 mm to more than 10 times the initial thickness. For larger deformations, one could observe secondary buckling along the outlines of the basic pattern (Figure 6a). The secondary buckling was characterized by the formation of fractal-like protrusions along the long-hanging walls. In all gels, the onset of secondary buckling was preceded by the development of the Rayleigh—Taylor instability-driven pattern of deformations.

We observed that viscoelastic gels with higher α values were prone to developing these fractal-like structures. As the crossover frequency decreased (increased relaxation time, $\tau_{\rm m}$), more intricate buckling patterns were observed. The amplitude of the perturbations increased as the modulus of the gel decreased and as the initial thickness increased. This trend implies that, for softer gels, a larger volume of material moved toward the long-hanging borders of the dimples, stretching far below the substrate (Figure 6b), while less material remained in the thin flat dimples, which we assume leads to an accumulation of tension in the system. Several previous studies have reported that when tension is present in a soft material system adhered to a rigid surface, instability occurs along the soft material-rigid substrate contact line, consistent with our experimental observations. However, in the case of viscoelastic gels, the tension in the system develops gradually [Figure 6a(i-iii)]. Therefore, the amplitude of this tensioninduced instability is a function of time associated with material properties. Hence, in Figure 6c, we compare the relaxation time, $\tau_{\rm m}$ with $\alpha = \rho gh/G_{\rm 0}$. We observe that at smaller $\tau_{\rm m}$ or α , gels are more rigid and secondary buckling does not occur. On the other hand, for softer gels, corresponding to larger values of $\tau_{\rm m}$ and α , wavy protrusions start to form near the center of the dish ("locally buckled" in Figure 6c). For even softer gels, buckling propagates to a wider area, as shown in Figure 6a,c as "globally buckled".

CONCLUSIONS

In this study, we present experimental observations and theoretical confirmation of the gravity-driven Rayleigh-Taylor instability of viscoelastic solid gels. Through linear stability analysis, we identified that the viscous effect decreases the most unstable (dimensionless) wavenumber N. Hence, for the viscoelastic Rayleigh-Taylor instability, we observe surface patterns that are distinct from those predicted by the elastic Rayleigh-Taylor instability. Furthermore, we suggest that the viscoelastic Rayleigh-Taylor mechanism is sensitive to the initial thickness of the slab (as visualized in Figure 4c). From this, we conclude that viscoelastic solids can be of use in pattern-forming applications due to their ability to hold their shape and show various surface patterns/textures and the tunability of their final resulting surface pattern with the additional parameter ζ . Also, the growth rate of the instability determined from the linear stability analysis qualitatively agreed with the experimental observations. A future study can attempt to quantitatively describe the wave growth and amplitude through a nonlinear analysis. We believe that a study probing the effect of the boundary shape (e.g., applying a wavy substrate) may produce a passively reconfigurable textured surface.

ASSOCIATED CONTENT

5 Supporting Information

The Supporting Information is available free of charge at https://pubs.acs.org/doi/10.1021/acs.langmuir.3c02564.

Additional details of shear rheology, image analysis methods, extended discussion of linear stability analysis, and choice of parameters in Figure 4 (PDF)

AUTHOR INFORMATION

Corresponding Authors

Janine K. Nunes — Department of Mechanical and Aerospace Engineering, Princeton University, Princeton, New Jersey 08544, United States; ⊙ orcid.org/0000-0002-1742-2934; Email: nunes@princeton.edu

Howard A. Stone — Department of Mechanical and Aerospace Engineering, Princeton University, Princeton, New Jersey 08544, United States; ⊙ orcid.org/0000-0002-9670-0639; Email: hastone@princeton.edu

Authors

Malcolm Slutzky — Department of Physics, Princeton University, Princeton, New Jersey 08544, United States; Present Address: James Franck Institute and Department of Physics, University of Chicago, Chicago, Illinois 60637, USA

Jonghyun Hwang — Department of Mechanical and Aerospace Engineering, Princeton University, Princeton, New Jersey 08544, United States; orcid.org/0000-0002-6575-0940

Complete contact information is available at: https://pubs.acs.org/10.1021/acs.langmuir.3c02564

Author Contributions

M.S. and J.H. contributed equally to this work. J.K.N. and H.A.S. directed the study. J.K.N., M.S., and J.H. designed the experiments and J.H. and M.S. performed the experiments. H.A.S. directed the modeling. J.H. performed modeling and conducted material characterization. M.S. performed the image processing. All authors analyzed the data and wrote the manuscript.

Notes

The authors declare no competing financial interest.

ACKNOWLEDGMENTS

We thank the Princeton Center for Complex Materials and MRSEC (NSF DMR-2011750) for supporting this work. J.H. acknowledges financial support from the Kwanjeong Educational Foundation.

REFERENCES

- (1) Skrzeszewska, P. J.; Sprakel, J.; de Wolf, F. A.; Fokkink, R.; Cohen Stuart, M. A.; van der Gucht, J. Fracture and Self-Healing in a Well-Defined Self-Assembled Polymer Network. *Macromolecules* **2010**, *43*, 3542–3548.
- (2) Guo, J.; Liu, M.; Zehnder, A. T.; Zhao, J.; Narita, T.; Creton, C.; Hui, C.-Y. Fracture mechanics of a self-healing hydrogel with covalent and physical crosslinks: A numerical study. *J. Mech. Phys. Solids* **2018**, 120, 79–95.
- (3) Gent, A. N.; Petrich, R. P.; Tabor, D. Adhesion of viscoelastic materials to rigid substrates. *Proc. R. Soc. London, Ser. A* **1969**, 310, 433–448
- (4) Gent, A. N. Adhesion and Strength of Viscoelastic Solids. Is There a Relationship between Adhesion and Bulk Properties? *Langmuir* **1996**, *12*, 4492–4496.

- (5) Autumn, K. Gecko Adhesion: Structure, Function, and Applications. MRS Bull. 2007, 32, 473-478.
- (6) Jerison, E. R.; Xu, Y.; Wilen, L. A.; Dufresne, E. R. Deformation of an Elastic Substrate by a Three-Phase Contact Line. *Phys. Rev. Lett.* **2011**, *106*, 186103.
- (7) Roy, R.; Seiler, R. L.; Weibel, J. A.; Garimella, S. V. Droplets on Soft Surfaces Exhibit a Reluctance to Coalesce due to an Intervening Wetting Ridge. *Adv. Mater. Interfaces* **2020**, *7*, 2000731.
- (8) Zavodnik, J.; Košmrlj, A.; Brojan, M. Rate-dependent evolution of wrinkling films due to growth on semi-infinite planar viscoelastic substrates. *J. Mech. Phys. Solids* **2023**, *173*, 105219.
- (9) Rayleigh. Investigation of the Character of the Equilibrium of an Incompressible Heavy Fluid of Variable Density. *Proc. London Math. Soc.* **1882**, *s1*–14, 170–177.
- (10) Taylor, G. I. The instability of liquid surfaces when accelerated in a direction perpendicular to their planes. I. *Proc. R. Soc. London, Ser. A* **1950**, *201*, 192–196.
- (11) Mora, S.; Phou, T.; Fromental, J.-M.; Pomeau, Y. Gravity Driven Instability in Elastic Solid Layers. *Phys. Rev. Lett.* **2014**, *113*, 178301.
- (12) Chakrabarti, A.; Mora, S.; Richard, F.; Phou, T.; Fromental, J.-M.; Pomeau, Y.; Audoly, B. Selection of hexagonal buckling patterns by the elastic Rayleigh-Taylor instability. *J. Mech. Phys. Solids* **2018**, 121, 234–257.
- (13) Aitken, L. S.; Wilson, S. D. R. Rayleigh-Taylor instability in elastic liquids. *J. Non-Newtonian Fluid Mech.* **1993**, 49, 13–22.
- (14) Tan, Z.; Wang, W. Instability solutions for the Rayleigh—Taylor problem of non-homogeneous viscoelastic fluids in bounded domains. *J. Math. Anal. Appl.* **2019**, *476*, 773–800.
- (15) Wang, W.; Zhao, Y. On the Rayleigh—Taylor instability in compressible viscoelastic fluids. *J. Math. Anal. Appl.* **2018**, *463*, 198–221.
- (16) Saasen, A.; Hassager, O. Gravity waves and Rayleigh Taylor instability on a Jeffrey-fluid. *Rheol. Acta* 1991, 30, 301-306.
- (17) Mora, S.; Andò, E.; Fromental, J.-M.; Phou, T.; Pomeau, Y. The shape of hanging elastic cylinders. *Soft Matter* **2019**, *15*, 5464–5473.
- (18) Piriz, A. R.; López Cela, J.; Serna Moreno, M. C.; Cortázar, O.; Tahir, N. A.; Hoffmann, D. H. H. A new approach to Rayleigh—Taylor instability: Application to accelerated elastic solids. *Nucl. Instrum. Methods Phys. Res., Sect. B* **2007**, 577, 250–256.
- (19) Tamim, S. I.; Bostwick, J. B. A dynamic analysis of the Rayleigh—Taylor instability in soft solids. *Extreme Mech. Lett.* **2020**, 40, 100940.
- (20) Gou, J. N.; Zan, W. T.; Sun, Y. B.; Wang, C. Linear analysis of Rayleigh-Taylor instability in viscoelastic materials. *Phys. Rev. E* **2021**, *104*, 025110.
- (21) Style, R. W.; Boltyanskiy, R.; Allen, B.; Jensen, K. E.; Foote, H. P.; Wettlaufer, J.; Dufresne, E. R. Stiffening solids with liquid inclusions. *Nat. Phys.* **2015**, *11*, 82–87.
- (22) Mazurek, P.; Vudayagiri, S.; Skov, A. L. How to tailor flexible silicone elastomers with mechanical integrity: a tutorial review. *Chem. Soc. Rev.* **2019**, *48*, 1448–1464.
- (23) Pandey, A.; Karpitschka, S.; Lubbers, L. A.; Weijs, J. H.; Botto, L.; Das, S.; Andreotti, B.; Snoeijer, J. H. Dynamical Theory of the Inverted Cheerios Effect. *Soft Matter* **2017**, *13*, 6000–6010.
- (24) Mark, J. E. Polymer Data Handbook; Oxford University Press, 1999.
- (25) Nase, J.; Lindner, A.; Creton, C. Pattern Formation during Deformation of a Confined Viscoelastic Layer: From a Viscous Liquid to a Soft Elastic Solid. *Phys. Rev. Lett.* **2008**, *101*, 074503.
- (26) Style, R. W.; Jagota, A.; Hui, C.-Y.; Dufresne, E. R. Elastocapillarity: Surface Tension and the Mechanics of Soft Solids. *Annu. Rev. Condens. Matter Phys.* **2017**, *8*, 99–118.
- (27) Chandrasekhar, S. *Hydrodynamic and Hydromagnetic Stability*; Dover Publications, 1961; pp 428–480.
- (28) Bellman, R.; Pennington, R. H. Effects of surface tension and viscosity on Taylor instability. Q. Appl. Math. 1954, 12, 151–162.

- (29) Ghatak, A.; Chaudhury, M. K.; Shenoy, V.; Sharma, A. Meniscus Instability in a Thin Elastic Film. *Phys. Rev. Lett.* **2000**, *85*, 4329–4332.
- (30) Biggins, J. S.; Mahadevan, L. Meniscus instabilities in thin elastic layers. *Soft Matter* **2018**, *14*, 7680–7689.

NOTE ADDED AFTER ASAP PUBLICATION

This paper was published on December 19, 2023. Equation 3 has been updated and the revised version was re-posted on December 20, 2023.